Nanoscale

PAPER

View Article Online
View Journal | View Issue

Cite this: *Nanoscale*, 2025, **17**, 16737

Adsorption and electron transfer of metal-reducing decaheme cytochrome protein MtrF on iron oxide nanoparticle surfaces†

Jiahuiyu Fang,[a] Pranab Sarker,[a,b] Xiaoxue Qin,[a] Shuting Zhang,[a,b] Size Zheng[c] and Tao Wei*[a,b]

Dissimilatory metal-reducing bacteria (DMRB) transfer electrons to extracellular metal oxides *via* a multiheme cytochrome network. Coupling DMRB with iron oxide nanoparticles (NPs) enables continuous redox processes for various applications such as bioremediation and bioenergy. The conformation of the terminal decaheme cytochrome MtrF on the surface critically influences electron transfer (ET) efficiency. In this work, we used molecular dynamics simulations and master equations to study MtrF adsorption on 3.6 and 6.0 nm α-Fe_2O_3 NPs and its steady-state ET in water. Our study shows that the heme cofactors can have strong electrostatic interactions with iron oxide NP surfaces, promoting protein adsorption and interfacial ET, while a small number of hydration water molecules in the first hydration shell of the iron oxide NP form hydrogen bonds with protein residues, stabilizing them near the NP surface. The NP adsorption sites, which are favorable for the interfacial ET, are located at the heme groups near the terminals of two intersecting heme chains. Among these sites, the region around hemes 4 and 5, near the terminal of the long heme chain, along with heme 7 at the terminal of the staggered cross short chain, is found to be relatively energetically favorable and ET-efficient, anchoring MtrF in a lie-down orientation on the NP. As the NP size increases, more protein residues adsorb onto the NP, potentially hindering heme attachment. The MtrF adsorption on the NP distorts its heme network and affects ET, but has a negligible effect on the protein's secondary structure. The kinetic behavior of ET across MtrF and the rate-limiting step are governed by heme–NP contacts, the ratio of electron injection to ejection rate constants, and the direction of ET. Our study of protein–NP interactions is important for the development of bionanotechnologies.

Received 9th May 2025,
Accepted 18th June 2025

DOI: 10.1039/d5nr01891a

rsc.li/nanoscale

1. Introduction

Redox reactions govern various energy-conversion processes in biology, such as respiration[1] that proceeds *via* electron transfer (ET) across biological molecules or the abiotic–biotic interface.[2] Dissimilatory metal-reducing bacteria (DMRB), *e.g.*, *Shewanella oneidensis* and *Geobacter metallireducens*, utilize a wide range of compounds as terminal electron acceptors for their anaerobic respiration.[3] Electrons are transferred from their cell's interior to mineral oxides, such as Fe(III) and Mn(III/IV) oxides, through the multiheme c-type cytochrome protein network. The protein MtrF, along with its analogues MtrC and OmcA, is a decaheme c-type cytochrome associated with the outer membrane of Fe(III)-respiring species of the *Shewanella* genus, mediating electron transfer directly to extracellular acceptors such as insoluble iron and manganese minerals.[4]

Metal oxide nanoparticles (NPs) coupled with DMRB can generate continuous redox processes for important applications in wastewater treatment,[5] bioremediation,[2] global biogeochemical cycles,[3] and energies.[6–9] For example, in DMRB-coupled engineered zero-valent iron NPs or low-valent iron oxide NPs, the reactive properties of Fe(0) and Fe(II) are utilized to degrade chlorinated organic compounds[10] and to convert hexavalent chromium (Cr(VI)) into non-toxic trivalent chromium (Cr(III)),[11] while the added DMRB can reduce and reactivate iron oxide particles, thereby creating continuous redox cycles. Microbial fuel cells (MFCs) can fulfill the dual task of wastewater treatment and electricity generation.[12] In MFCs, hematite iron oxide (α-Fe_2O_3) NPs can be used to modify the anode surface to

[a]*Department of Biomedical Engineering, University of South Carolina, Columbia, South Carolina, 29208, USA. E-mail: taow@mailbox.sc.edu*
[b]*Department of Chemical Engineering, University of South Carolina, Columbia, South Carolina, 29208, USA. E-mail: taow@mailbox.sc.edu*
[c]*Department of Chemistry, Stony Brook University, Stony Brook, New York, 11794, USA*

† Electronic supplementary information (ESI) available. See DOI: https://doi.org/10.1039/d5nr01891a

enhance the *Shewanella* putrefaciens DMRB attachment, increase the extracellular ET,[13–15] and improve electricity generation (maximum power density of ~4.92 W m^{-2}).[6,16] The cytochrome protein's structures and orientations and the substrate surface's properties govern the ET efficiency.[17]

Extensive studies have attempted to elucidate the binding mechanisms of extracellular ET proteins on iron oxide acceptors. Previous experimental studies[18] demonstrated the direct ET mechanism, *i.e.*, the electron transfer by the multiheme cytochrome protein complex MtrCBA across the outer membrane of *Shewanella oneidensis* through contact between the transmembrane protein complex MtrCAB and the surface of α-Fe_2O_3 NPs. Experiments[19] of two-dimensional IR correlation showed that the binding groups from OmcA to α-Fe_2O_3 were in the sequence of carboxyl groups, amide II, and amide I. Recent experiments[20] employed protease footprinting techniques to show that the binding site of MtrF to 27 nm α-Fe_2O_3 NPs is located in a specific region near hemes 6 and 7, driven by the electrostatic interactions between the binding regions of MtrF and α-Fe_2O_3 NPs.

Extensive computational effort has also been made to understand the ET mechanism within the heme network of multiheme cytochromes and at the protein–NP/surface interface.[15,18,21–31] The ET hopping rate constant k_{ij} across the neighboring hemes i and j, or the abiotic–biotic interface, can be estimated using Marcus theory:[32]

$$k_{ij} = \frac{2\pi}{\hbar}\left\langle |H_{ij}|^2 \right\rangle \frac{1}{\sqrt{4\pi\lambda k_B T}} \exp\left(-\frac{(\Delta G_{ij}+\lambda)^2}{4\lambda k_B T}\right) \quad (1)$$

where H_{ij}, λ, and ΔG_{ij} are the electronic coupling elements, reorganization energy, and reaction free energy, respectively. Among these, the electronic coupling strength is the most critical in determining the ET rate, requiring calculations at the quantum level. There are different methods to estimate the electronic coupling matrix elements. These include but are not limited to the block diagonalization[25] generalized Mulliken–Hush (GMH) method,[26] fragment charge difference,[27] fragment energy difference,[28] projection methods,[29] fragment orbital density functional theory (FODFT),[30] constrained density functional theory (CDFT),[23,31] FODFT combined with CDFT,[33] and ultrafast parametrized methods.[34] The coupling strength can also be approximated[22] as $H_{ij} \approx \exp[-r\beta/2]$, where r is the heme-to-heme distance or distance between the substrate and the protein or *vice versa*. β is a constant, which can be obtained from the fitted values in the dissociation curve available in the literature.[22,35]

The net electron flux across the heme network can be simulated by solving the master equations[22] or using the kinetic Monte Carlo (KMC) method,[36,37] with electron hopping rates estimated from the aforementioned quantum mechanical simulations. By solving master equations for electron hopping along the heme network, an intrinsic, maximum possible electron flux through solvated MtrF of 10^4–10^5 s^{-1} was found, consistent with the recent experimentally measured rates for the related multiheme cytochrome protein complex MtrCAB.[22] Another prior investigation used KMC simulations and single-molecule scanning tunnelling microscopy experiments to explore the outer membrane decaheme cytochrome MtrF of *Shewanella oneidensis* MR-1, revealing a rich phase diagram of the overall electron occupation density of the hemes as a function of electron injection and ejection rates.[37] Our previous simulation study using the combination of atomistic molecular dynamics (MD) simulations, free energy calculations, and KMC simulations[36] showed that the terminal group of heme 5 of the MtrF protein orients toward the Au(111) surface due to the large surface tension of the gold surface, the strong gold–thiol interaction, and π–π interactions between the aromatic group and the gold surface. The kinetics of ET across the MtrF protein is governed by the structure and orientation of the surface.[36]

Despite previous extensive efforts on both theoretical and experimental fronts, the molecular mechanism of the adsorption and ET of multiheme cytochrome proteins on iron oxide NP surfaces remains elusive. It is of paramount importance to meet the demands of practical applications requiring sufficient ET efficiency at abiotic–biotic interfaces. In this study, we investigated the adsorption of MtrF on α-Fe_2O NPs of varying sizes using atomistic MD simulations, a widely used approach for probing bio-interfacial behavior at atomic resolution.[2,38–50] We identified protein binding sites, which are favorable for the interfacial ET. Based on the simulated conformation of the adsorbed protein, we also analyzed the steady-state ET kinetics across MtrF adsorbed on the NP surface by solving master equations using the parameters of electron hopping rates based on the Marcus theory,[32] which were reported in the literature.[22] MtrF is chosen because it serves as an extracellular conduit in *Shewanella*, facilitating electron transfer from cells to iron oxide surfaces.

2. Computational details

2.1. Molecular dynamics simulations

MD simulations were carried out to study the MtrF adsorption on α-Fe_2O_3 NPs in the *NVT* ensemble with periodic boundary conditions. The velocity Verlet algorithm was applied with a time step of 1.0 fs to resolve trajectories in MD simulations. The system's temperature was maintained at 298.15 K using a velocity-rescale thermostat. The simulations were performed using the software of GROMACS (version 2019.6),[51] along with the CHARMM36 force field[52] and the TIP3P water model. The structure of the complete sequence (see the ESI†) of *Shewanella oneidensis* cytochrome MtrF (PDB code: 3PMQ) was predicted using the I-TASSER server.[53] The MtrF protein was assigned a net charge of −36 e based on the protonation and deprotonation states of its amino acid residues in water. 36 Na^+ counterions were added to the system to neutralize the system at pH 7.0. The MtrF protein was solvated for 200 ns before interacting with the α-Fe_2O_3 NP.

Two NPs with diameters of 3.6 nm and 6.0 nm (Fig. 1b) were generated directly from an α-Fe_2O_3crystal, with the stoichiometric ratio of Fe to O atoms set to 2 : 3, similar to previous atomistic MD simulation studies of iron oxide NPs[54] and

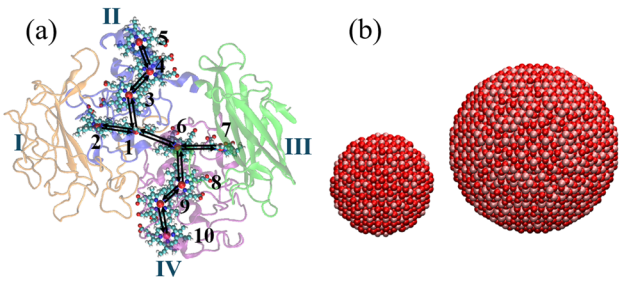

Fig. 1 (a) The solvated configuration of MtrF, along with the ET path through the network of heme cofactors (cyan). The four domains of MtrF (I, II, III, and IV) are colored sequentially from the N-terminus to the C-terminus in orange, blue, green, and purple, respectively. For the heme groups, Fe ions are colored red, whereas the C atoms are colored cyan, the N atoms are colored blue, the O atoms are colored red, and the H atoms are colored white. The arrows represent the electron transfer steps between heme i and heme j with reaction rates k_{ij}. (b) (Left) 3.6 nm and (right) 6 nm α-Fe_2O_3 NPs. In the NPs, the Fe atoms are colored pink and the O atoms are colored red.

iron oxide surfaces.[55] The positions of NP atoms were fixed in the simulations. The force field parameters for the interactions between Fe_2O_3 NPs and proteins were adopted from the literature[56] (see Table S1 in the ESI† for more details). Those parameters were estimated from density functional theory (DFT) and calibrated with experiments, although the polarization was not presented explicitly in the current model.[56]

To analyze binding sites while eliminating protein–protein interaction effects, MD simulations of single MtrF protein adsorption on a 3.6 nm α-Fe_2O_3 NP in water were performed in a 15 × 15 × 15 nm^3 box. Five independent simulation runs were performed in each case to ensure statistical reliability. A single MtrF protein was randomly positioned near the NP surface, with different heme groups oriented toward the NP and an initial minimum heme–NP distance of approximately 0.3 nm. To investigate the effect of NP size on adsorption behavior, we also used a 6 nm α-Fe_2O_3 NP, with hemes 4 and 5 initially positioned close to the NP surface in water, in a box of 17 × 17 × 17 nm^3. All our MD simulations were run for over 200 ns and the equilibration of these simulations was determined when the distance between the hemes and the NP and the total energy reached a plateau over time. Since the time required to reach equilibration varies across different cases, we adopted a consistent approach by selecting the final 20 ns of each trajectory after reaching the equilibration for all subsequent analyses. Additionally, a system comprising three MtrF molecules was constructed. Initially, the three MtrF proteins were spatially separated and positioned at least 0.8 nm from the surface of the 3.6 nm NP. The simulation box size was 18 × 18 × 18 nm^3 and the entire system was equilibrated for 200 ns.

2.2. Master equations for electron transfer at the steady state

The steady-state dynamic behaviors of electron transfer across the MtrF protein were analyzed by solving the master equations of ET flux at the steady state (see the details in the ESI†). In this process, MtrF is modeled as a 10-site electron-hopping network, where each heme group is indexed from 1 to 10, as shown in Fig. 1. The i-th heme group can either be occupied, with an occupation probability denoted by P_i. Specifically, P_i = 1 indicates that the electron entry site i is occupied (*i.e.*, the i-th heme contains Fe^{2+}), while P_i = 0 indicates that it is unoccupied (corresponding to Fe^{3+}). The initial heme network is assumed to be empty. All possible ETs between heme pairs are shown in Fig. 1a. The flux of electron transfer from heme i to heme j, J_{ji}, is described by the following chemical master equation:

$$J_{ji} = k_{ji}P_i(1 - P_j) \tag{2}$$

where k_{ji} is the ET rate from hemes i to j; heme i and heme j act as the electron donor and receptor, respectively. The net ET flux from hemes i to j is described as:

$$J_{ji} + J_{ij} = k_{ji}P_i(1 - P_j) - k_{ij}P_j(1 - P_i) \tag{3}$$

The injected electron flux J_{in} and the ejected electron flux J_{out} at the input and output sites, respectively, can be expressed by the following equations:

$$J_{in} = k_{in}(1 - P_{in}) \tag{4}$$

$$J_{out} = k_{out}(1 - P_{out}) \tag{5}$$

In the steady state, all ET fluxes are equal. The overall time-averaged electron occupation density $\langle P \rangle$ was calculated through:

$$\langle P \rangle = \frac{\sum_{i=1}^{10} P_i}{10} \tag{6}$$

The ET rate constant k_{ij} was determined using the non-adiabatic rate equation derived from the Marcus theory[32] according to eqn (1). In our work, the values of λ and ΔG_{ij} were taken from the literature.[22] The electronic coupling matrix element H_{ij} was estimated as follows:

$$\left\langle |H_{ij}|^2 \right\rangle^{\frac{1}{2}}(r) = A \exp\left[\frac{-\beta(r - r_0)}{2}\right] \tag{7}$$

where r is the edge-to-edge distance between hemes i and j, A = 3.77 meV, r_0 = 3.6 Å and β = 1.65 $Å^{-1}$ according to the literature.[22,35] Eqn (7) with the fitting parameters[22] can reasonably reproduce $|H_{ij}|$ data for MtrF obtained using the fragment-orbital density functional theory (FODFT) method within a QM/MM scheme. As our work involves MtrF, we utilized these fitting parameters to avoid fine-tuning the parameters in empirical approaches or the computational cost involved in the *ab initio* methods to estimate $|H_{ij}|$. The steady-state ET kinetics, including the electron density and flux of MtrF adsorbed on the NPs, were obtained by solving the master equations. The detailed solution steps are provided in the ESI.†

3. Results and discussion

3.1. Single-protein adsorption on a 3.6 nm NP

Fig. 1a shows the solvated structure of the MtrF protein with its complete amino acid sequence. MtrF contains four domains: domains I and III are primarily composed of β-sheet structures, while domains II and IV are rich in α-helices. The decaheme cofactors of MtrF are arranged in a staggered cross configuration, forming two intersecting chains of hemes. This unique structure facilitates efficient and reversible electron transfer. Heme 5 in domain II and heme 10 in domain IV are located at opposite terminals along the main chain of heme cofactors in the MtrF protein (Fig. 1a). Importantly, in the transmembrane MtrFED complex of *Shewanella oneidensis*, heme 10 in MtrF functions as an extracellular interface for interacting with external electron acceptors such as mineral particles, suggesting its key role in the initial or final electron exchange events.[56] In contrast, heme 5, located at the interface between MtrF and MtrD, plays a complementary role in distributing or collecting electrons within the heme network of the bacteria.[56] Heme 2 and heme 7, positioned at the opposite terminals of the other orthogonal short chain (Fig. 1a), can also participate in interfacial electron exchange. As shown in our previous study[38] of MtrF adsorption on the Au(111) surface, the orientation of the heme network, particularly the terminal hemes 5 and 10 along the main chain, is the key to ET across the MtrF protein between the aqueous environment and the substrate gold surface.

To study the interactions between single MtrF proteins and α-Fe_2O_3 NPs, and to identify adsorption sites favorable for the interfacial ET between the protein's heme network and the iron oxide NP surface, an MtrF protein was initially positioned with its heme groups facing the NP. We set up different simulations using initial configurations near the heme groups that are exposed to water. For each configuration, we performed five independent simulation runs with different initial velocities to ensure statistical robustness. Interactions at different locations along the heme network were then analyzed to identify the strongest adsorption sites, while the shortest heme–NP surface distance was measured to rationalize the interfacial ET (Table 1). Multiple simulations with different initial atomic velocities were performed to validate the result of the preferable adsorption sites. For example, as shown in Fig. 2a, the region of hemes 4 and 5 near the terminal (Fig. 1a) is initially close to the NP. At 320 ns, after the rotation, hemes 4, 5, and 7 were adsorbed, within which hemes 4 and 5 were the most preferable based on the heme-to-NP distance (Fig. 2b) and protein–NP interactions (Table 1).

To determine the closest heme sites at a given time t, the minimum distance d between different hemes within the protein and the NP was tracked throughout the simulation (Fig. 2a). Hemes 4 and 5 are found to have the shortest distance (~0.22 nm) to the NP surface, which is 0.14 nm shorter

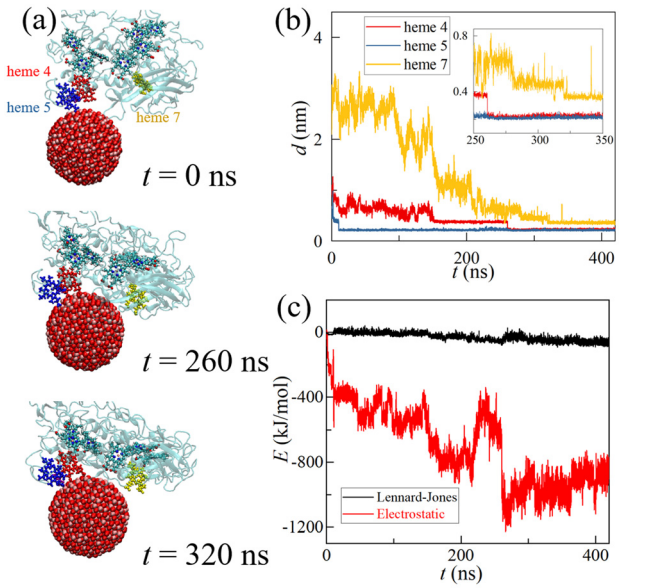

Fig. 2 MtrF adsorption on the 3.6 nm NP: hemes 4 (red) and 5 (blue) are initially close to the α-Fe_2O_3 NP, with the final adsorption occurring at hemes 4, 5, and 7 (yellow). (a) Snapshots of the initial position of MtrF (at t = 0 ns) and the adsorption process at 200 ns and 320 ns. (b) Time evolution of the minimum distances of heme 4 (red line), heme 5 (blue line), and heme 7 (yellow line) to the NP. A zoomed-in view of the energy fluctuations is shown in the inset. (c) Time evolution of interaction energies (Lennard-Jones and electrostatics) between the NP and MtrF (including the heme cofactors).

Table 1 Summary of the minimum distance (d) and interaction energies (electrostatic (E_{elect}) and LJ (E_{LJ})) between the different adsorption sites of MtrF on α-Fe_2O_3 NPs of different sizes

Initial site	Adsorption site	NP size (nm)	d (Å)	E_{elect} (kJ mol^{-1})	E_{elect} Percentage	E_{LJ} (kJ mol^{-1})
Hemes 4/5	Hemes 4/5/7	3.6	2.2 ± 0.1 (heme 4) 2.2 ± 0.1 (heme 5) 3.6 ± 0.1 (heme 7)	−866.81 ± 46.75	98% (heme) 2% (protein)	−59.09 ± 13.97
Hemes 4/5	Hemes 4/5/7	6.0	3.8 ± 0.2 (heme 4) 3.9 ± 0.4 (heme 5) 4.3 ± 0.2 (heme 7)	−493.66 ± 82.47	24% (heme) 76% (protein)	−68.21 ± 12.63
Heme 10	Hemes 9/10	3.6	3.8 ± 0.2 (heme 9) 3.4 ± 0.2 (heme 10)	−896.27 ± 119.98	17% (heme) 83% (protein)	−43.32 ± 15.77
Heme 2	Heme 2	3.6	4.1 ± 0.4 (heme 2)	−489.40 ± 52.52	25% (heme) 75% (protein)	−14.43 ± 8.32

than the distance involving heme 7 (Table 1). In fact, it is the shortest distance among all adsorption sites observed in our simulations (Table 1). When comparing the adsorption kinetics, different kinetics for different heme groups are observed, even for hemes 4 and 5, which have a similar initial distance to the NP surface (Fig. 2b). As shown in Fig. 2a, upon adsorption, the MtrF protein rotates around the α-Fe_2O_3 NP and lies down on its surface.

Fig. 2c shows the time evolution of the electrostatic and Lennard-Jones (LJ) interaction energies between MtrF (including the heme cofactors) and the α-Fe_2O_3NP. As the protein is fully adsorbed onto the NP surface, both energies are negative (Fig. 2c), indicating that the underlying interactions between MtrF and the NP are attractive. The average electrostatic energy (−866.81 kJ mol^{-1}) is significantly greater than the LJ interaction energy (−59.09 kJ mol^{-1}) (see Table 1). When comparing the individual heme contribution to the total electrostatic interactions, the highest contribution comes from heme 4 (−547.22 kJ mol^{-1}). Another significant contribution (−386.26 kJ mol^{-1}) comes from heme 5. However, unlike hemes 4 and 5, the contribution of heme 7 is repulsive but relatively small (28.44 kJ mol^{-1}). As a result, the minimum distance d is 1.4 Å larger than those of hemes 4 and 5. Due to the strong attractive interaction with the NP, hemes 4 and 5 remain close to the NP, while heme 7 stays approximately 3.6 Å away and exhibits slightly larger fluctuations on the NP surface due to its positive interactions (*i.e.*, slight repulsion), which causes the protein to orient itself along the curvature of the NP (Fig. 2a). The 98% contribution of hemes 4, 5, and 7 to the total electrostatic interaction (Table 1) supports the conclusion that the interactions between these hemes and the NP govern the protein's lie-down orientation, while the role of protein residues is insignificant in this case.

We also measured the distances between Fe and O atoms in the 3.6 nm NP and atoms in hemes 4, 5, and 7. It was found that the interatomic distance between the Fe atoms of the NP and the O atoms of hemes 4 and 5 is 1–1.5 Å shorter than that between the O atoms of the NP and the O atoms of hemes 4 and 5. This suggests that the O atoms in hemes 4 and 5 bind to oppositely charged Fe atoms on the NP surface, resulting in an attractive force. In contrast, the closest O atoms of heme 7 are near the O atoms on the NP, which leads to a repulsive force between heme 7 and the NP. These findings demonstrate that while the net electrostatic attraction drives MtrF onto the NP, the local interactions of heme groups with the NP surface influence both the heme-NP distances and the local mobilities of those heme groups, as evidenced by the different distance fluctuations of hemes 4, 5, and 7 at equilibrium. We observed a larger fluctuation of d for heme 7 than for others, as shown in the inset of Fig. 2b.

Apart from the aforementioned initial configuration, we also position hemes 6 and 7 close to the NP (Fig. 3a), mimicking the experimental observation that the adsorption sites of MtrF on a 27 nm NP are near hemes 6 and 7.[20] Our simulation shows that despite starting from a different initial configuration, the regions at hemes 4, 5, and 7 consistently emerge as the preferred adsorption site (Fig. 3). The discrepancy between

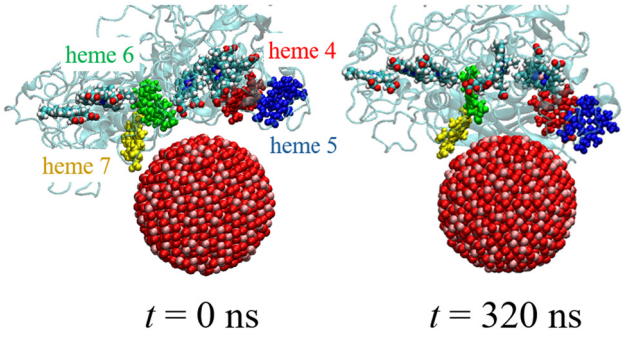

Fig. 3 MtrF adsorption on the 3.6 nm α-Fe_2O_3 NP: hemes 6 (green) and 7 (yellow) are initially near the NP surface, while the final adsorption sites are heme 4 (red), heme 5 (blue), and 7 (yellow). Two configurations for the initial position (0 ns) and the final adsorption position (320 ns).

our simulations and a previous experimental report[20] may arise from multiple factors. The diameter of our simulated NP is only 3.6 nm, which is much smaller than that used in the experiment (27 nm).[20] As shown in our previous studies[57] on protein adsorption on NPs, a difference in the NP curvature results in distinct protein adsorption orientations. Additionally, real iron oxide NPs possess amorphous surface structures and complex terminations due to oxidation and hydroxylation, which differ from the perfect NP model used in our simulation.

However, when the terminal hemes of MtrF (hemes 10 and 2) are initially positioned near the NP, alternative adsorption sites are observed. For instance, placing heme 10 close to the NP results in an adsorption involving hemes 9 and 10 (Fig. S3†). In this case, the protein–NP interaction energy reaches −896.27 kJ mol^{-1} (Table 1), but the minimum distances to the NP surface from heme 9 and heme 10 are 0.38 nm and 0.34 nm, respectively, both of which are larger than those involving hemes 4 and 5. Therefore, the sites of hemes 9/10 are relatively less efficient in the ET than the sites of hemes 4/5/7. Notably, the contribution from hemes 9/10 to the electrostatic interactions decreases to 17%, while the overall protein–NP electrostatic interactions increase to 83%.

In another case, when heme 2 is initially placed close to the NP (Fig. S4†), the minimum heme–NP distance increases to 0.41 nm, which is the largest among all the cases (Table 1). The total interaction energy for heme 2 adsorption—considering both the protein and heme contributions—is still less than that for the adsorption of hemes 4/5/7 (Table 1). As the heme–NP distance increases, more amino acid residues of the MtrF protein contribute to the interaction. Among them, residue GLU109 dominates, accounting for approximately 75% of the total adsorption energy (Table 1).

3.2. Size effect on the protein–NP interactions

We further investigated the effect of NP size on MtrF adsorption using a larger 6.0 nm α-Fe_2O_3 NP (Fig. 4). For a consistent comparison, we adopted the same initial configuration involving hemes 4, 5, and 7 as used with the smaller 3.6 nm NP. In

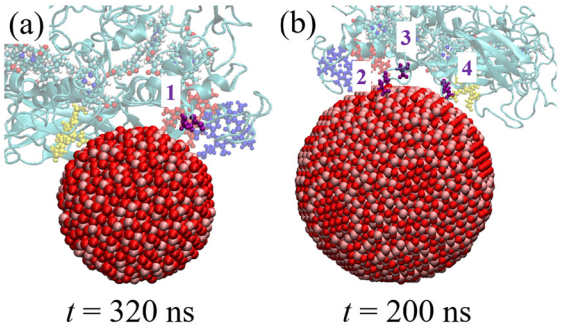

Fig. 4 (a) MtrF Adsorption on the 3.6 nm α-Fe_2O_3 NP when the initial sites are hemes 4 (red) and 5 (blue); final sites are hemes 4 (red), 5 (blue), and 7 (yellow). Adsorbed residue 1: GLN280 at 320 ns. (b) Adsorption of MtrF on the 3.6 nm NP with adsorbed residues (residue 2: GLU440; residue 3: GLU443, and residue 4: ARG426) at 200 ns. The cutoff distance for determining the residue adsorption is 4 Å.

this case, the regions at hemes 4, 5, and 7 remain the preferred adsorption sites. However, the minimum distance is larger and the interaction energy is 43% weaker than that around the adsorption site of hemes 4/5/7 (Table 1). Unlike with the smaller 3.6 nm NP, the protein becomes the main contributor to the total interaction with the NP due to the adsorption of additional amino acid residues on the larger NP. As seen in Fig. 4, a single residue of GLN280 is adsorbed on the 3.6 nm NP (Fig. 4a), while additional residues, including GLU440, GLU443, and ARG426, are adsorbed on the 6.0 nm NP (Fig. 4b). Energy analyses show that the electrostatic interaction (−493.66 kJ mol^{-1}) between the NP and the protein, including heme cofactors, is an order of magnitude greater than its van der Waals interactions (−43.32 kJ mol^{-1}) (Table 1). However, the heme–NP contribution accounts for only 24% of the total electrostatic interaction (Table 1).

Fig. 5a shows the radial distribution function $g(r) = \rho(r)/\rho_{bulk}$, which represents the ratio between the water local density $\rho(r)$ at the radial distance r and the bulk water density ρ_{bulk}. A strong primary hydration peak (the first hydration peak at $r \sim 1.9$ Å) appears approximately 3 Å from the 6.0 nm α-Fe_2O_3 NP surface,

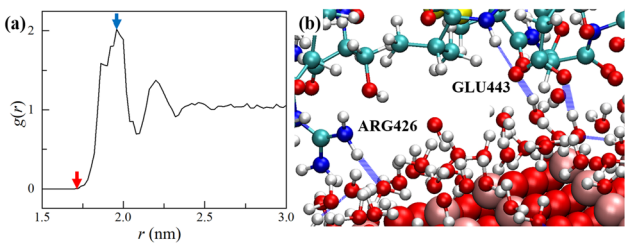

Fig. 5 Hydration and residue adsorption of the 6.0 nm α-Fe_2O_3 NP. (a) Radial distribution function $g(r)$ of water molecules on the NP surface. The spherical origin of $g(r)$ is the NP center. The red arrow indicates the surface of the NP and the blue arrow indicates the peak of the first hydration. (b) Hydrogen bonding between MtrF and the water molecules adsorbed on the NP surface. The water layer is defined using a cutoff distance of 3 Å from the NP surface. The blue dashed lines represent hydrogen bonds.

indicating that the NP surface is covered by a condensed water layer containing approximately 1190 water molecules. Approximately 307 hydrogen bonds are observed between the hydrogen atoms of surface-bound water molecules (representing ~25.8% of the total water molecules in the first hydration shell of the 6.0 nm NP) and the oxygen atoms on the surface of the iron oxide NP. These surface-adsorbed water molecules can also form hydrogen bonds with the nearby amino acid residues, helping to maintain the stability of the adsorbed protein on the NP surface. Fig. 5b shows an example of the formed hydrogen bonds between the hydrogen atoms of residues GLU443 and ARG426 near the 6.0 nm NP surface and the oxygen atoms of water molecules in the first hydration layer for the 6.0 nm NP. However, the average number of hydrogen bonds between the protein residues and the surface-bound water in the NP's first hydration shell is only approximately 4.7; in contrast, on the smaller 3.6 nm NP, it is less than 2.8 (see the details in Table S2 in the ESI†). The small number of hydrogen bonds suggests that they contribute minimally to the total protein–NP interaction, although they can mediate the adsorption of nearby residues and affect their local stability on the NP surface. Moreover, our simulations show that there are no hydrogen bonds between the iron oxide NP and the protein residues or heme cofactors.

3.3. Multiprotein–NP interactions

We examined the adsorption of multiple MtrF proteins on the 3.6 nm α-Fe_2O_3 NP. Initially, the proteins were randomly placed at least 0.8 nm away from the NP. To focus on the interactions between the protein's heme cofactor and the NP, which is critical for the interfacial ET, the heme networks were initially oriented toward the NP surface. Fig. 6a shows the equilibrated conformation of three MtrF proteins on the 3.6 nm α-Fe_2O_3 NP in a water environment; Fig. 6b–d display the detailed adsorption sites of MtrF. As expected, the formation of an MtrF protein corona on the NP (*i.e.*, a protein layer on the NP surface)[57–59] is observed (Fig. 6a). Due to

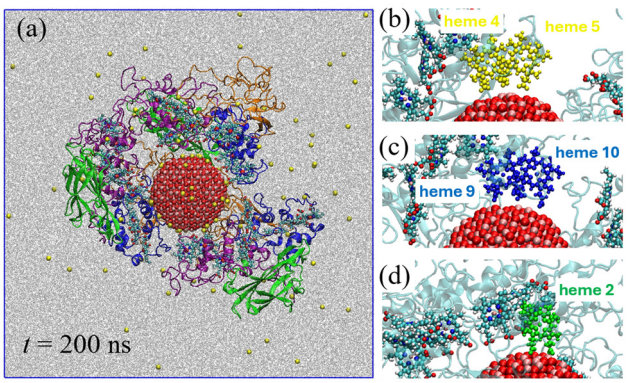

Fig. 6 (a) The initial configuration of three MtrFs surrounding the 3.6 nm α-Fe_2O_3 NP in water with counter ions (Na^+). The water molecules and the counter ions (Na^+) are colored grey and yellow, respectively. The adsorption configurations with (b) hemes 4 and 5 (yellow), (c) hemes 9 and 10 (blue), and (d) heme 2 (green). The MtrF is colored light blue in (b–d).

protein–protein interactions, the adsorbed proteins adopt different orientations on the NP surface. However, similar to the cases of single-protein adsorption, the regions at hemes 4/5, hemes 9/10, and heme 2 (Fig. 6c) remain in the preferred adsorption sites. Therefore, it is reasonable to conclude that our simplified single-MtrF adsorption simulations capture the essential features of the underlying interactions between MtrF and the NP, even in more realistic and complex scenarios where protein–protein interactions are inevitable. Accordingly, the ET rates estimated from the single-protein adsorption configuration with the shortest heme–NP distance would be a reliable estimation of the kinetics of ET across an adsorbed MtrF on the NP, which will be discussed in the following.

3.4. Kinetics of electron transfer across an adsorbed MtrF on the NP surface

In our earlier discussion, we demonstrated that the region around hemes 4/5/7 is the most preferred adsorption site during the interaction between MtrF and α-Fe_2O_3 NPs. It is also an ET-efficient adsorption site, because hemes 4 and 5 have close contact with the α-Fe_2O_3 NP (Table 1). Therefore, we treated it as a representative case for studying the steady-state ET kinetics for the adsorbed MtrF protein on the NP surface. Additionally, we compared the ET kinetics of the adsorption site hemes 4/5/7 with that of another site, hemes 9/10, which also exhibits strong protein–NP interactions.

In solving the master equations, we chose the configurations of MtrF simulated from MD simulations. As mentioned earlier, for the adsorption site of hemes 4/5/7, the distance between heme 7 and the NP surface is 3.6 Å, which is larger than the distance of 2.2 Å for hemes 4 and 5 (see the configuration in Fig. 2 and Table 1). The electron hopping rate constant k_{ij} was calculated based on the edge-to-edge distance between neighboring hemes i and j using eqn (1) and (7) (see the Computational details section for details). According to eqn (7), H_{ij} decays exponentially with the distance between heme 7 and the NP, resulting in a smaller H_{ij} value for heme 7 compared to hemes 4 and 5, and indicating a weaker ET at the interface involving heme 7. In addition, as mentioned above, heme 7 exhibits repulsive interactions with the NP, which leads to a relatively greater local mobility on the NP surface than hemes 4 and 5. Therefore, in our analysis, we consider only the ET between the terminal groups of hemes 4 and 5, which are tightly adsorbed onto the NP surface, and the terminal group of heme 10, which is exposed to the aqueous environment. Fig. 7a shows the three-dimensional electron occupancy density $\langle n \rangle$ (top panel) and electron flux J (bottom panel) as a function of the two injection rates ($k_{4,\mathrm{in}}$ and $k_{5,\mathrm{in}}$) for hemes 4 and 5 and the one ejection rate of $k_{10,\mathrm{out}}$ for heme 10.

As the electron hopping rate constants $k_{4,\mathrm{in}}$, $k_{5,\mathrm{in}}$ and $k_{10,\mathrm{out}}$ vary, three distinct phases are observed in the time-averaged occupation density $\langle n \rangle$ and the net flux J of MtrF (Fig. 6). When ET is limited by the injection rate constants (*i.e.*, when the values of $k_{4,\mathrm{in}}$ and $k_{5,\mathrm{in}}$ are smaller than that of $k_{10,\mathrm{out}}$), the system enters a low-density (LD) phase (Fig. 7a). In this phase, the electrons in the heme network are depleted and the heme sites are predominantly oxidized. Conversely, when the electron hopping rate constants $k_{4,\mathrm{in}}$ and $k_{5,\mathrm{in}}$ are much larger than $k_{10,\mathrm{out}}$, the system transitions to a high-density (HD) phase (Fig. 7a) and the heme network becomes saturated with electrons, *i.e.*, the Fe atoms in the heme sites are mostly reduced. In both the LD and HD phases, the ET within the heme network is limited, resulting in a very low flux (Fig. 7c). When the $k_{4,\mathrm{in}}$, $k_{5,\mathrm{in}}$ and $k_{10,\mathrm{out}}$ values exceed the smallest intra-heme ET hopping rate constant along the multiheme pathway, the system reaches the maximum current (MC) phase

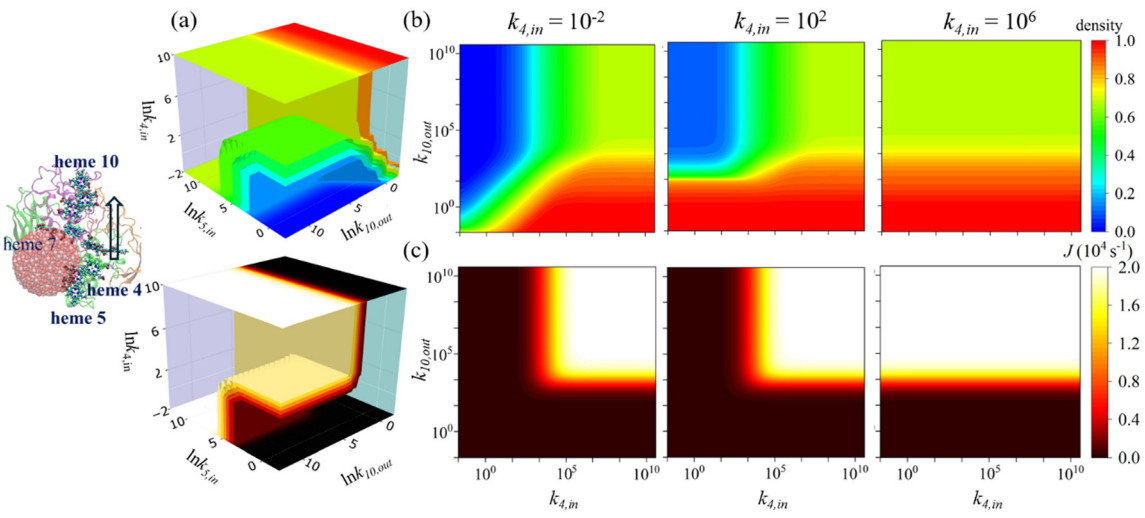

Fig. 7 Kinetics of the ET across the adsorbed MtrF on the α-Fe_2O_3 NP along the direction from hemes 4/5 to heme 10. (a) 3D phase diagram of the time-averaged electron occupancy density $\langle n \rangle$ and the net electron flux J across the MtrF as a function of the electron hopping rate constants for two injection sites: $k_{4,\mathrm{in}}$ for heme 4 and $k_{5,\mathrm{in}}$ for heme 5, and the electron hopping rate constant $k_{10,\mathrm{out}}$ for the electron ejection site at heme 10. (b) 2D phase diagrams of $\langle n \rangle$ and (c) J as a function of $k_{5,\mathrm{in}}$ and $k_{10,\mathrm{out}}$ at three values of $k_{4,\mathrm{in}}$: 10^{-2} s^{-1}, 10^{2} s^{-1}, and 10^{6} s^{-1}.

(Fig. 7a). In this phase, electrons are efficiently transported through the heme network, resulting in the highest flux and maximum electron transport efficiency. These three phases are similar to the previous results of single-electron injection and single-electron ejection obtained through KMC simulations.[36,37] A similar ET kinetic behavior in the opposite direction, *i.e.*, from heme 10 to hemes 4/5, is also observed, as illustrated in Fig. S5 of the ESI.†

The 3D ET behavior (Fig. 7a) can be better understood by investigating the 2D figures (Fig. 7b and c), in which the $k_{4,in}$ values were set to 10^{-2} s^{-1}, 10^{2} s^{-1}, and 10^{6} s^{-1}, respectively. As the $k_{4,in}$ value increases from 10^{-2} to 10^{6} s^{-1}, the LD region in the electron density phase diagram gradually diminishes, while the HD region (Fig. 7b) expands correspondingly. When the $k_{4,in}$ value reaches 10^{6} s^{-1}, the phase diagram consists solely of the HD and MC regions, separated at $k_{10,out} \sim 10^{3}$ s^{-1} (Fig. 7b, for $k_{4,in} = 10^{6}$ s^{-1}). This occurs because a sufficiently large $k_{4,in}$ value ensures a continuous and stable supply of electrons from heme 4 to the network. The LD phase, previously attributed to limited electron input and depletion along the ET pathway, is no longer present. When the sole output parameter $k_{10,out}$ is not sufficiently larger than $k_{4,in}$, an excessive electron influx causes persistent blockage within the pathway, leading to an HD state (Fig. 7b, for $k_{4,in} = 10^{6}$ s^{-1}). However, when $k_{10,out}$ dominates over $k_{4,in}$, the system reaches its maximum flux, corresponding to the MC state (Fig. 7b, for $k_{4,in} = 10^{6}$ s^{-1}). The variation in the $k_{4,in}$ value is manifested as a gradual expansion of the high electron flux region in the electron flux phase diagram (Fig. 7c), aligning with the corresponding changes in electron density.

We calculated the maximum ET rate for the solvated MtrF structure and the adsorbed MtrF structures on the NP surface (Table 2). The comparison of the maximum ET flux J values for both cases shows that the direction of the maximum value of J is reversed in both cases, consistent with our previous findings for MtrF adsorbed onto a gold surface,[38] which suggests that the NP–MtrF interactions also change the time-limiting steps. For example, for the solvated structure, the maximum ET flux rate for the forward direction (heme 5 → heme 10) is 7.4×10^{3} s^{-1}, with the rate-limiting step being heme 1 → heme 6, as shown in Table 2. In the reverse direction (heme 10 → heme 5), the rate-limiting step is reversed (heme 6 → heme 1), with the maximum ET flux being 1.3×10^{4} s^{-1} and larger than that of the forward direction (Table 2). However, in the adsorbed structure with hemes 4 and 5 being the adsorption sites, the opposite trend is observed (Table 2). The rate-limiting steps are also heme 3 → heme 1 and heme 8 → heme 6 for the forward and reverse directions, respectively (Table 2).

For the conformation of the adsorption site with hemes 9/10, electrons are transferred between hemes 9/10 and heme 5. The maximum flux J for the transfer from heme 5 to hemes 9/10 is close to that in the reverse direction. For the ET in the forward and reverse directions, the rate-limiting steps are heme 3 → heme 1 and heme 8 → heme 6, respectively, which differ from the solvated structure (Table 2). These results indicate that the NP–protein interaction alters the heme network structure (to be discussed further later), ultimately reversing the maximum ET flux.

In the literature,[18,60–64] the reported values of ET rate constant k_{ij} between a cytochrome protein and the Fe_2O_3 NP/surface vary widely. It depends on the type of cytochrome, the mineral phase of Fe_2O_3 NPs, and the electron acceptors (NPs or the surface). For example, the measured k_{ij} value is 10^{-4} s^{-1} between c-type cytochrome and γ-Fe_2O_3 NPs.[60] In the case of c-type cytochromes MtrC and OmcA from *Shewanella oneidensis* MR-1 and α-Fe_2O_3 NPs, the ET k_{ij} values are 0.26 s^{-1} for MtrC[63] and 0.11 s^{-1} for OmcA.[61–63] On the other hand, the estimated ET rate constant values range from 1 to 10^{4} s^{-1} and 0.01 to 20 s^{-1} for exothermic and endothermic driving forces, respectively, between the cytochrome of *Shewanella oneidensis* and the α-Fe_2O_3 surface.[65] The $k_{4,in}$ values (10^{-2} s^{-1} and 10^{4} s^{-1}) used in Fig. 7b are within the measured[61–63] and estimated range.[65] For these $k_{4,in}$ values, the calculated maximum ET flux J rates are in the order of 10^{3}–10^{4} s^{-1} and match the measured value for the ET rate from MtrCAB in a proteoliposome to an α-Fe_2O_3 surface electron acceptor.[18] It is also consistent with the value obtained in the maximum current phase within MtrF in KMC simulations for the MtrF in the bulk.[36]

As mentioned above, the NP–MtrF interaction can perturb the heme network within the protein, influencing the optimal direction of electron transfer. To quantify the perturbations in the MtrF heme network caused by the NP, we compared it with the solvated counterpart, as illustrated in Fig. 8. Specifically, we calculated the ratio δ between the differences in edge-to-edge pairwise heme distances in the solvated ($d_{0,ij}$) and adsorbed (d_{ij}) proteins to the edge-to-edge pairwise heme distances in the solvated protein using the following equation:

$$\delta = \frac{d_{ij} - d_{0,ij}}{d_{0,ij}} \times 100\% \quad (8)$$

We observed both increment (red) and reduction (blue) of heme–heme pairwise distances, as shown in Fig. 8. For example, the distance between heme 3 and heme 4 increases, while it

Table 2 Maximum electron flux (s^{-1}) and rate-limiting step between hemes 5 and 10 for different adsorption sites, averaged over 10 configurations

		Maximum electron flux, $\times 10^{3}$ J (s^{-1})		Rate-limiting step	
Configurations		Heme 5 → heme 10	Heme 10 → heme 5	Heme 5 → heme 10	Heme 10 → heme 5
Solvated		7.4 ± 0.6	13 ± 1	Heme 1 → heme 6	Heme 6 → heme 1
Adsorbed	Hemes 4 and 5	20 ± 4	10 ± 3	Heme 3 → heme 1	Heme 8 → heme 6
	Hemes 9 and 10	9.3 ± 2.2	8.0 ± 4.1	Heme 3 → heme 1	Heme 8 → heme 6

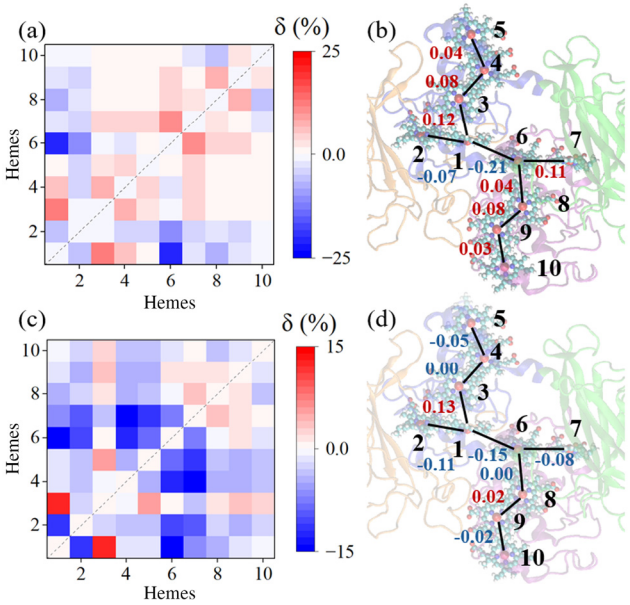

Fig. 8 Heme-to-heme network distortions compared to the solvated structures. (a) Distortion matrix and (b) heme network with hemes 9 and 10 being adsorbed on the NP. (c) Distortion matrix and (d) heme network with hemes 4, 5, and 7 being adsorbed on the NP. *x*- and *y*-axes represent hemes 1–10. The color scale indicates the degree of pairwise heme distance distortions obtained using eqn (8): red represents an increase, while blue indicates a decrease. (b) and (d) map these distance variations onto the MtrF network, highlighting only heme pairs involved in ET. Distances that increase upon NP adsorption are labeled in red, while those that decrease are labeled in blue. The numerical values denote the relative change in heme-to-heme distances between the adsorbed and solvated structures.

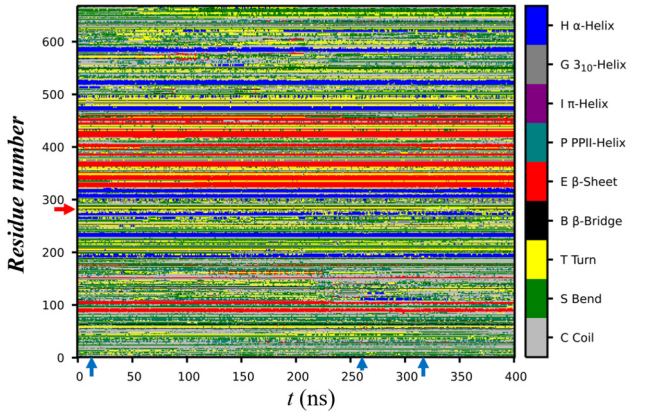

Fig. 9 Time evolution of the secondary structures in the case where hemes 4, 5, and 7 are adsorbed onto the 3.6 nm NP. The red arrow indicates the residue (GLN280) adsorbed on the NP surface, defined as being within 4 Å of the surface. The blue arrows indicate the adsorption time for heme 5 (10 ns), heme 4 (260 ns), and heme 7 (320 ns).

decreases between heme 1 and heme 6. However, the largest change (δ) we obtain is the 21% reduction in the distance between heme 1 and heme 6 with hemes 9 and 10 being the adsorbed sites (Fig. 8a and b). This large reduction could be the primary reason for the observed shift in the rate-limiting steps, from heme 1 → heme 6 in the solvated MtrF to heme 3 → heme 1 in the adsorbed MtrF and from heme 6 → heme 1 in the solvated MtrF to heme 8 → heme 6 in the adsorbed MtrF, along the forward and reverse ET directions, respectively (Table 2). It could also be the reason for the higher maximum electron transfer rate, J, in the forward ET direction (9.3×10^3 s^{-1}) compared to the reverse ET direction (8.0×10^3 s^{-1}) (Table 2). Similarly, the reversal of the maximum flux direction (Table 2) is observed in the case of the adsorption sites at hemes 4 and 5, for which a 15% reduction in the distance between heme 1 and heme 6 is identified (Fig. 8c and d).

The secondary structures of the adsorbed MtrF protein were monitored. As shown in Fig. 9, the secondary structure of MtrF on the NP surface remains stable during the adsorption process. Our results are consistent with a previous study[17] of MtrF adsorption on a gold surface. The structural stability of MtrF is critical for ensuring robust and sustained extracellular electron transfer. We also analyzed the secondary structures of MtrF in other cases, including the adsorption at the sites of hemes 4/5/7 on the larger 6.0 nm NP, as well as at the sites of hemes 9/10, and the site of heme 2 on the smaller 3.6 nm NP (Fig. S6†). In all cases, adsorption onto the NP resulted in negligible changes to the protein's secondary structure.

It is worth noting that the adsorption behavior of MtrF on α-Fe_2O_3 NPs in this study differs from that on the Au(111) surface.[36] Our previous study[36] showed that dehydration of the gold surface, driven by high surface tension, promotes protein adsorption, while π–π interactions help stabilize the adsorbed protein. On the Au(111) surface, a single adsorption site, heme 10, was identified. In contrast, the present study reveals multiple adsorption sites on the α-Fe_2O_3 NP and explores ET in a multiple-input, multiple-output heme network.

4. Conclusions

The coupling of DMRB with iron oxide particles can generate a continuous redox process for various advanced applications in bioremediation, bioenergy, and biosensing. Understanding the adsorption and ET behaviors of metal-reducing proteins is crucial for developing efficient bionanotechnologies. In this work, we investigated the adsorption and ET behaviors of the metal-reducing decaheme protein MtrF on small α-Fe_2O_3 NPs in an aqueous environment using atomistic MD simulations.

The feasible NP adsorption sites, which are favorable for the interfacial ET between the heme cofactor and the NP surface, are found at the heme groups near the terminals of two intersecting heme chains of MtrF. Among these, on the surface of small-sized NPs with a diameter of 3.6 nm, the region around hemes 4 and 5 at the terminal of the long heme chain, along with heme 7 at the terminal of the orthogonal short chain, exhibits relatively strong interactions with the NP. At this binding site, the protein adopts a lie-down orientation on the NP surface. This site also shows the shortest heme–NP distance, which is favorable for interfacial ET between the NP

surface and the heme groups of MtrF. The region around hemes 9 and 10, located near the opposite terminus of the long chain, also shows strong NP adsorption, involving more amino acid residues but exhibiting larger heme–NP distances than the region near hemes 4 and 5, potentially reducing the interfacial ET efficiency. The site at heme 2, near the terminal of the orthogonal short chain, shows approximately 50% lower protein–heme interactions and an 88% larger heme–NP distance compared to the site of hemes 4/5/7, making it less favorable for interfacial ET.

Our study reveals that the main driving force for the protein adsorption is the electrostatic interaction between the NP and the heme groups or protein residues. Water molecules bound to the NP surface can form hydrogen bonds with nearby residues; however, their contribution to local adsorption is minimal due to the limited number of hydrogen bonds. An increase in NP size introduces more protein residues on the surface and increases the heme–NP distance, which can decrease interfacial ET.

Furthermore, we analyzed the case with the highest ET activity (*i.e.*, the adsorption site of hemes 4/5/7) and solved using the master equation within the heme network to examine the ET behavior at the steady state. While the adsorption of MtrF on the NP surface has a negligible effect on the protein's secondary structure, it distorts the heme network and alters the rate-limiting step within the heme network. This effect leads to a larger value of the maximum ET flux in the hemes 4/5 → heme 10 direction compared to the reverse direction. Our fundamental study of protein–NP interactions and their effect on the ET kinetics for an adsorbed protein are crucial for the future development of DMRB-driven bionanotechnologies, particularly in the areas of environmental and energy applications.

Author contributions

Jiahuiyu Fang: conceptualization, investigation, formal analysis, methodology, visualization, data curation, and writing – original draft. Pranab Sarker: formal analysis, methodology, visualization, validation, supervision, and writing – original draft. Xiaoxue Qin: methodology, formal analysis, and visualization. Shuting Zhang: formal analysis, visualization, and validation. Tao Wei: conceptualization, investigation, formal analysis, methodology, validation, visualization, data curation, project administration, resources, funding acquisition, supervision, and writing – review & editing.

Conflicts of interest

There are no conflicts to declare.

Data availability

The authors confirm that the data supporting the findings of this study are available within the article and its ESI.†

Acknowledgements

TW acknowledges the support from the National Science Foundation (award # 2400531 (original #: 1943999)) and the University of South Carolina. TW is grateful for the support of computational resources at the Texas Advanced Computing Center (TACC). The simulations were performed at the HPCs of Frontera at TACC, Expanse at San Diego Supercomputer Center (SDSC) and Hyperion at the University of South Carolina.

References

1 T. Wei, M. A. Carignano and I. Szleifer, *Langmuir*, 2011, **27**, 12074–12081.
2 C. M. Nakano, H. S. Byun, H. Ma, T. Wei and M. Y. El-Naggar, *Comput. Phys. Commun.*, 2015, **193**, 1–9.
3 L. Shi, H. Dong, G. Reguera, H. Beyenal, A. Lu, J. Liu, H.-Q. Yu and J. K. Fredrickson, *Nat. Rev. Microbiol.*, 2016, **14**, 651–662.
4 D. Coursolle and J. A. Gralnick, *Front. Microbiol.*, 2012, **3**, 56.
5 N. A. Baker, D. Sept, S. Joseph, M. J. Holst and J. A. McCammon, *Proc. Natl. Acad. Sci. U. S. A.*, 2001, **98**, 10037–10041.
6 S. Pandit, S. Khilari, S. Roy, D. Pradhan and D. Das, *Bioresour. Technol.*, 2014, **166**, 451–457.
7 S. Cestellos-Blanco, H. Zhang, J. M. Kim, Y.-x. Shen and P. Yang, *Nat. Catal.*, 2020, **3**, 245–255.
8 A. Vázquez-Arias, J. Pérez-Juste, I. Pastoriza-Santos and G. Bodelon, *Nanoscale*, 2021, **13**, 18054–18069.
9 J. Li, H. Han, Y. Chang and B. Wang, *Nanoscale*, 2023, **15**, 6009–6024.
10 H. Zhong, H. Lyu, Z. Wang, J. Tian and Z. Wu, *Chemosphere*, 2024, 141505.
11 T. Zhang, H. Li, Y. Wu, Y. Yuan and Y. Du, *Biodegradation*, 2025, **36**, 1–14.
12 R.-B. Song, C.-E. Zhao, L.-P. Jiang, E. S. Abdel-Halim, J.-R. Zhang and J.-J. Zhu, *ACS Appl. Mater. Interfaces*, 2016, **8**, 16170–16177.
13 F. Liu, A. E. Rotaru, P. M. Shrestha, N. S. Malvankar, K. P. Nevin and D. R. Lovley, *Environ. Microbiol.*, 2015, **17**, 648–655.
14 R. Wang, H. Li, J. Sun, L. Zhang, J. Jiao, Q. Wang and S. Liu, *Adv. Mater.*, 2021, **33**, 2004051.
15 X. Jiang, B. Burger, F. Gajdos, C. Bortolotti, Z. Futera, M. Breuer and J. Blumberger, *Proc. Natl. Acad. Sci. U. S. A.*, 2019, **116**, 3425–3430.
16 B. Cao, Z. Zhao, L. Peng, H.-Y. Shiu, M. Ding, F. Song, X. Guan, C. K. Lee, J. Huang and D. Zhu, *Science*, 2021, **373**, 1336–1340.
17 H. C. Watanabe, Y. Yamashita and H. Ishikita, *Proc. Natl. Acad. Sci. U. S. A.*, 2017, **114**, 2916–2921.
18 G. F. White, Z. Shi, L. Shi, Z. Wang, A. C. Dohnalkova, M. J. Marshall, J. K. Fredrickson, J. M. Zachara, J. N. Butt

and D. J. Richardson, *Proc. Natl. Acad. Sci. U. S. A.*, 2013, **110**, 6346–6351.
19 S.-S. Yu, J.-J. Chen, R.-F. Cheng, Y. Min and H.-Q. Yu, *Environ. Sci. Technol.*, 2021, **55**, 11424–11433.
20 T. Fukushima, S. Gupta, B. Rad, J. A. Cornejo, C. J. Petzold, L. J. G. Chan, R. A. Mizrahi, C. Y. Ralston and C. M. Ajo-Franklin, *J. Am. Chem. Soc.*, 2017, **139**, 12647–12654.
21 T. A. Clarke, M. J. Edwards, A. J. Gates, A. Hall, G. F. White, J. Bradley, C. L. Reardon, L. Shi, A. S. Beliaev and M. J. Marshall, *Proc. Natl. Acad. Sci. U. S. A.*, 2011, **108**, 9384–9389.
22 M. Breuer, K. M. Rosso and J. Blumberger, *Proc. Natl. Acad. Sci. U. S. A.*, 2014, **111**, 611–616.
23 M. Melander, E. O. Jónsson, J. J. Mortensen, T. Vegge and J. M. García Lastra, *J. Chem. Theory Comput.*, 2016, **12**, 5367–5378.
24 Z. Futera and J. Blumberger, *J. Phys. Chem. C*, 2022, **126**, 3301–3303.
25 T. Pacher, L. Cederbaum and H. Köppel, *Chem. Phys.*, 1988, **89**, 7367–7381.
26 R. J. Cave and M. D. Newton, *Chem. Phys. Lett.*, 1996, **249**, 15–19.
27 A. A. Voityuk and N. Rösch, *Chem. Phys.*, 2002, **117**, 5607–5616.
28 C.-P. Hsu, Z.-Q. You and H.-C. Chen, *J. Phys. Chem. C*, 2008, **112**, 1204–1212.
29 A. Migliore, S. Corni, R. Di Felice and E. Molinari, *Chem. Phys.*, 2006, **124**, 064501.
30 K. Senthilkumar, F. Grozema, F. Bickelhaupt and L. Siebbeles, *Chem. Phys.*, 2003, **119**, 9809–9817.
31 Q. Wu and T. Van Voorhis, *Chem. Phys.*, 2006, **125**, 164105.
32 R. A. Marcus and N. Sutin, *Biochim. Biophys. Acta, Rev. Bioenerg.*, 1985, **811**, 265–322.
33 H. Oberhofer and J. Blumberger, *Chem. Phys.*, 2010, **133**, 244105.
34 F. Gajdos, S. Valner, F. Hoffmann, J. Spencer, M. Breuer, A. Kubas, M. Dupuis and J. Blumberger, *J. Chem. Theory Comput.*, 2014, **10**, 4653–4660.
35 M. Breuer, P. Zarzycki, J. Blumberger and K. M. Rosso, *J. Am. Chem. Soc.*, 2012, **134**, 9868–9871.
36 T. Wei, H. Ma and A. Nakano, *J. Phys. Chem. Lett.*, 2016, **7**, 929–936.
37 H. S. Byun, S. Pirbadian, A. Nakano, L. Shi and M. Y. El-Naggar, *ChemElectroChem*, 2014, **1**, 1932–1939.
38 T. Zhang, T. Wei, Y. Han, H. Ma, M. Samieegohar, P.-W. Chen, I. Lian and Y.-H. Lo, *ACS Cent. Sci.*, 2016, **2**, 834–842.
39 H. Huang, C. Zhang, R. Crisci, T. Lu, H.-C. Hung, M. S. J. Sajib, P. Sarker, J. Ma, T. Wei and S. Jiang, *J. Am. Chem. Soc.*, 2021, **143**, 16786–16795.
40 X. Qin, J. Fang, A. A. Chen, P. Sarker, M. S. J. Sajib, M. J. Uline and T. Wei, *Langmuir*, 2024, **41**, 1005–1012.
41 P. Sarker, G. T. Chen, M. S. J. Sajib, N. W. Jones and T. Wei, *Colloids Surf., A*, 2022, **653**, 129943.
42 N. P. Van Der Munnik, M. S. J. Sajib, M. A. Moss, T. Wei and M. J. Uline, *J. Chem. Theory Comput.*, 2018, **14**, 2696–2704.
43 Z. A. Gandhi, T. Lu, W. Guo, R. Crisci, J. Gao, M. C. Wilson, C. R. So, P. Sarker, X. Qin and T. Wei, *J. Phys. Chem. Lett.*, 2025, **16**, 4031–4037.
44 S. Zheng, P. Sarker, D. Gursoy, T. Wei and B. S. Hsiao, *Langmuir*, 2025, 9369–9376.
45 C. M. Nakano, H. Ma and T. Wei, *Appl. Phys. Lett.*, 2015, **106**, 153701.
46 T. Wei, T. Huang, B. Qiao, M. Zhang, H. Ma and L. Zhang, *J. Phys. Chem. B*, 2014, **118**, 13202–13209.
47 M. S. J. Sajib, Y. Wei, A. Mishra, L. Zhang, K.-I. Nomura, R. K. Kalia, P. Vashishta, A. Nakano, S. Murad and T. Wei, *Langmuir*, 2020, **36**, 7658–7668.
48 S. C. Mandal, R. Sarangi and A. Acharya, *J. Chem. Inf. Model.*, 2025, 4568–4575.
49 J. Zhou, J. Zheng and S. Jiang, *J. Phys. Chem. B*, 2004, **108**, 17418–17424.
50 X. Lin, K. Lin, S. He, Y. Zhou, X. Li and X. Lin, *Langmuir*, 2023, **39**, 11621–11627.
51 B. Hess, C. Kutzner, D. Van Der Spoel and E. Lindahl, *J. Chem. Theory Comput.*, 2008, **4**, 435–447.
52 J. Huang, S. Rauscher, G. Nawrocki, T. Ran, M. Feig, B. L. De Groot, H. Grubmüller and A. D. MacKerell Jr, *Nat. Methods*, 2017, **14**, 71–73.
53 X. Zhou, W. Zheng, Y. Li, R. Pearce, C. Zhang, E. W. Bell, G. Zhang and Y. Zhang, *Nat. Protoc.*, 2022, **17**, 2326–2353.
54 C. Moya, R. Escudero, D. C. Malaspina, M. De La Mata, J. Hernández-Saz, J. Faraudo and A. Roig, *ACS Appl. Bio Mater.*, 2019, **2**, 3084–3094.
55 P. N. Acero, S. Mohr, M. Bernabei, C. Fernández, B. Dominguez and J. P. Ewen, *Langmuir*, 2021, **37**, 14582–14596.
56 K. Kanhaiya, M. Nathanson, P. J. in't Veld, C. Zhu, I. Nikiforov, E. B. Tadmor, Y. K. Choi, W. Im, R. K. Mishra and H. Heinz, *J. Chem. Theory Comput.*, 2023, **19**, 8293–8322.
57 M. S. J. Sajib, P. Sarker, Y. Wei, X. Tao and T. Wei, *Langmuir*, 2020, **36**, 13356–13363.
58 P. Sarker, M. S. J. Sajib, X. Tao and T. Wei, *J. Phys. Chem. B*, 2022, **126**, 601–608.
59 G. T. Chen, P. Sarker, B. Qiao and T. Wei, *J. Nanopart. Res.*, 2023, **25**, 108.
60 I. A. Modenez, L. J. Macedo, A. F. Melo, A. R. Pereira, O. N. Oliveira Jr and F. N. Crespilho, *J. Colloid Interface Sci.*, 2021, **599**, 198–206.
61 Y. Xiong, L. Shi, B. Chen, M. U. Mayer, B. H. Lower, Y. Londer, S. Bose, M. F. Hochella, J. K. Fredrickson and T. C. Squier, *J. Am. Chem. Soc.*, 2006, **128**, 13978–13979.
62 C. M. Eggleston, J. Vörös, L. Shi, B. H. Lower, T. C. Droubay and P. J. Colberg, *Inorg. Chim. Acta*, 2008, **361**, 769–777.
63 L. Shi, D. J. Richardson, Z. Wang, S. N. Kerisit, K. M. Rosso, J. M. Zachara and J. K. Fredrickson, *Environ. Microbiol. Rep.*, 2009, **1**, 220–227.
64 D. M. A. Smith, K. M. Rosso, M. Dupuis, M. Valiev and T. P. Straatsma, *J. Phys. Chem. B*, 2006, **110**, 15582–15588.
65 S. Kerisit, K. M. Rosso, M. Dupuis and M. Valiev, *J. Phys. Chem. C*, 2007, **111**, 11363–11375.